Supporting information: Three-dimensional Quantification of the Facet Evolution of Pt Nanoparticles in a Variable Gaseous Environment

Thomas Altantzis[1,‡], Ivan Lobato[1,‡], Annick De Backer[1], Armand Béché[1], Yang Zhang[1], Shibabrata Basak[2], Mauro Porcu[2], Qiang Xu[2], Ana Sánchez-Iglesias[3], Luis M. Liz-Marzán[3,4], Gustaaf Van Tendeloo[1], Sandra Van Aert[1] and Sara Bals[1]*

[1]Electron Microscopy for Materials Research (EMAT), University of Antwerp, Groenenborgerlaan 171, 2020 Antwerp, Belgium

[2]DENSsolutions, Informaticalaan 12, Delft, 2628ZD, The Netherlands

[3]Bionanoplasmonics Laboratory, CIC biomaGUNE, Paseo de Miramón 182, 20014 Donostia - San Sebastian, Spain

[4]Ikerbasque, Basque Foundation for Science, 48013 Bilbao, Spain

*e-mail: sara.bals@uantwerpen.be

Table of contents

S1. Colloidal synthesis of Pt NPs

Chemicals: Potassium tetrachloroplatinate (II) (K_2PtCl_4), tetradecyltrimethylammonium bromide and sodium borohydride ($NaBH_4$) were purchased from Sigma-Aldrich. All chemicals were used as received. Milli-Q water (resistivity 18.2 MΩ·cm at 25 °C) was used in all experiments.

Synthesis of platinum cubes: Platinum NPs were prepared in a scintillation vial (20 mL) by reduction of K_2PtCl_4 with freshly prepared $NaBH_4$ in an aqueous tetradecyltrimethylammonium bromide solution.[1]

Initially, aqueous solutions of K_2PtCl_4 (0.1 mL, 100 mM) and tetradecyltrimethylammonium bromide (9.9 mL, 100 mM) were mixed at room temperature. The mixture was heated at 50 ºC

for 5 min in an oil bath, and $NaBH_4$ (0.3 mL, 1 M) was added under vigorous stirring. The flask was immediately closed with a septum and the resulting pressure inside the reaction flask was released by inserting a needle into the septum. After 10 min, the needle was removed, and the solution was stored at 50 ºC for 5 h under gentle stirring. The product was centrifuged at 5000 rpm for 30 min. The supernatant solution was separated and centrifuged again at 12000 rpm for 10 min. The precipitate was re-dispersed in 1 mL of water. The final size of platinum cubes was 9.7 ± 0.3 nm, as determined by TEM.

S2. High resolution TEM (HRTEM) imaging of Pt NPs

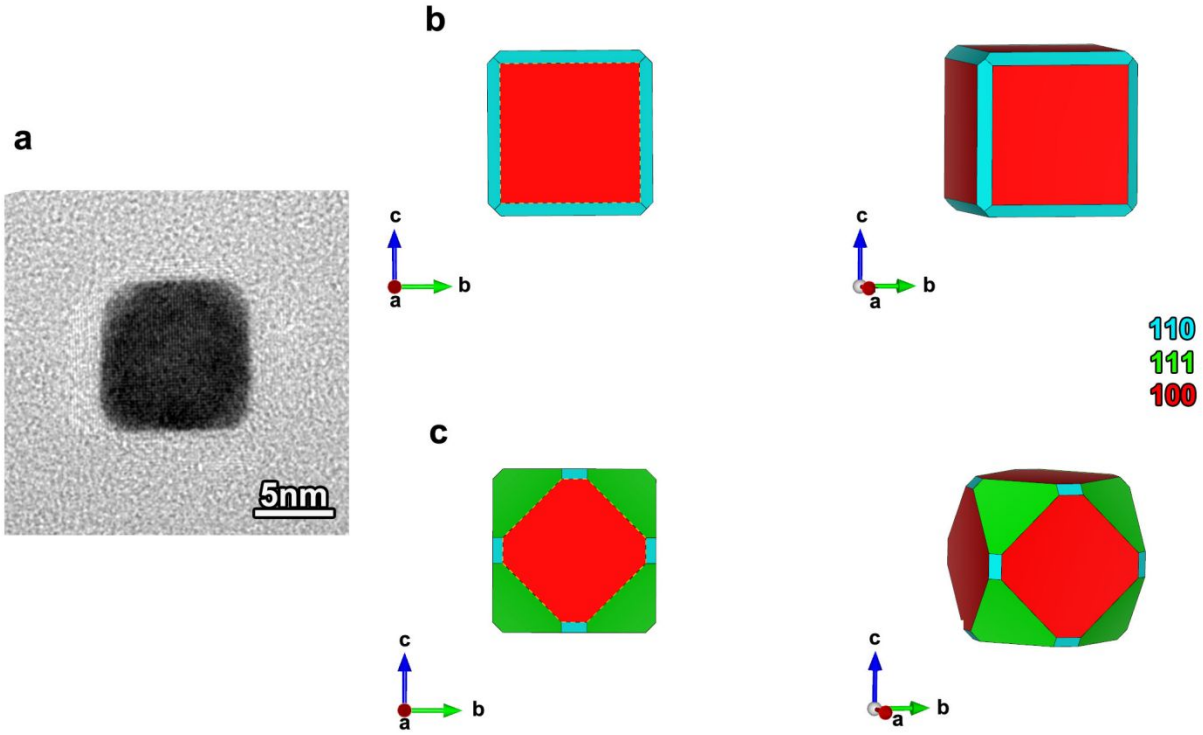

Figure S1 (a) HRTEM image of a Pt NP at room temperature oriented along a <100> zone axis and (b-c) two different models for the 3D shape of the NP based on the orientation and the

projected shape. It is clearly impossible to decide which of the two models describes the shape better, due to the lack of thickness information along the viewing direction.

S3. *In situ* aberration corrected HAADF-STEM observations

Experimental details

In situ observations of the shape evolution of Pt NPs were carried out using an aberration-corrected FEI-Titan Cubed electron microscope, operated at 300 kV. For HAADF-STEM, a probe convergence semi-angle of 21 mrad and detector inner and outer collection semi-angles of 42 and 95 mrad respectively, were used. The gas and heating cell holder (Climate S3+, DENSsolutions) is made of two chips functionalized with electron-transparent SiNx windows.[2,3] The thickness of the window membrane was approximately 30 nm. The temperature of the sample is accurately controlled via a 4-point probe method. The as-prepared Pt NPs were studied at 300 ˚C under 1 bar O_2 (99.999%) and 1 bar 5%H_2/Ar. To minimize the effect of the electron beam, the electron dose was reduced to 5580 $e^-/Å^2$, which is approximately 1 to 2 orders of magnitude lower in comparison to conventional HAADF-STEM imaging. Moreover, the dose rate was reduced by acquiring multiple frames with a short dwell time (0.25 μs) and a low beam current of 55 pA. The focus of the images was optimized to yield highest contrast.[4] To rule out any effect of the electron beam during our observations, we always compared the illuminated particles to those that were not exposed to the electron beam during the switch to a different gaseous environment and a similar particle shape was observed.

Structural characterization of Pt NPs at room temperature and ultra-high vacuum and at 300 ºC and under 5%H_2/Ar and O_2 flow

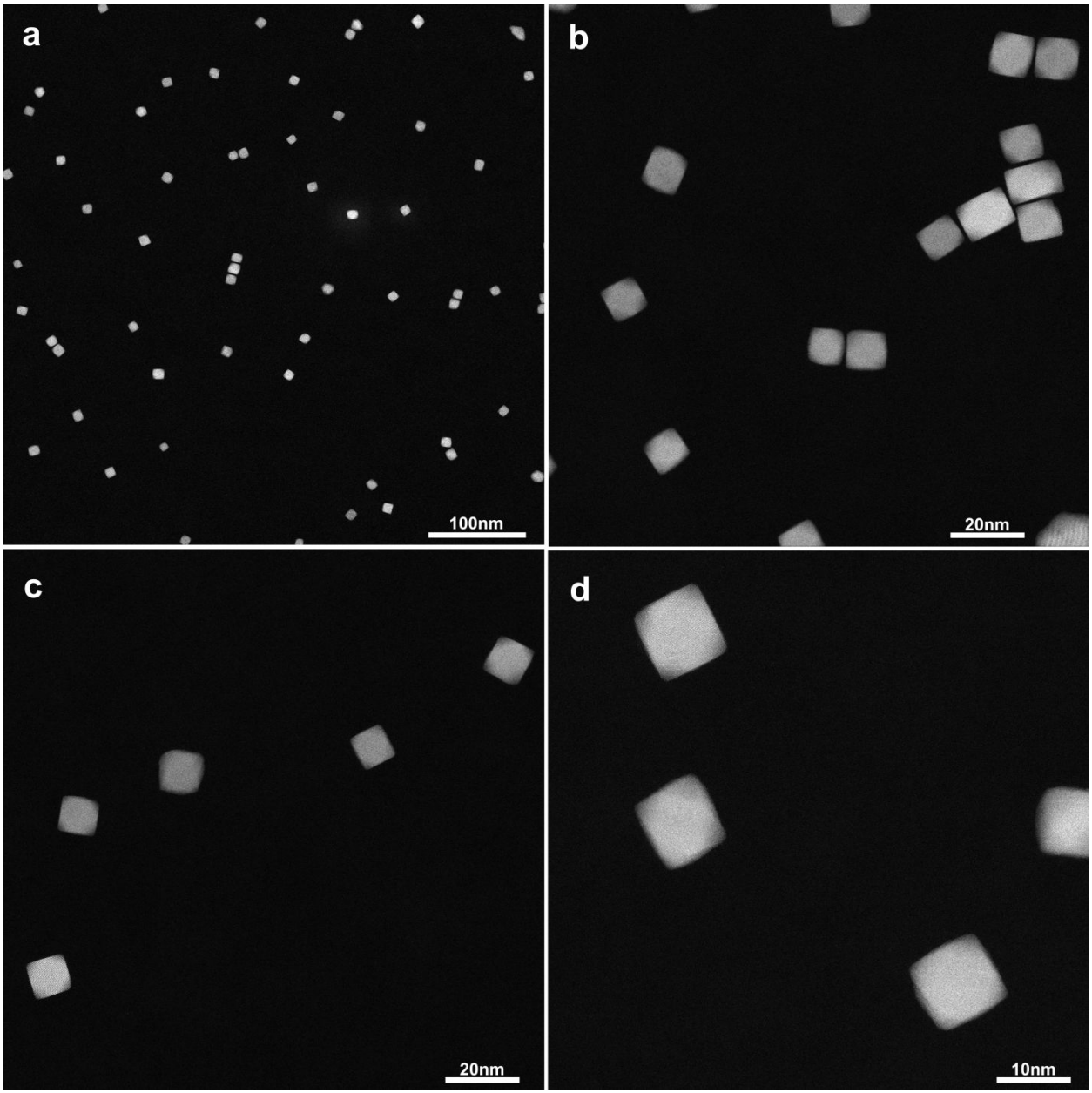

Figure S2. HAADF-STEM overview images of Pt NPs at room temperature and in ultra-high vacuum.

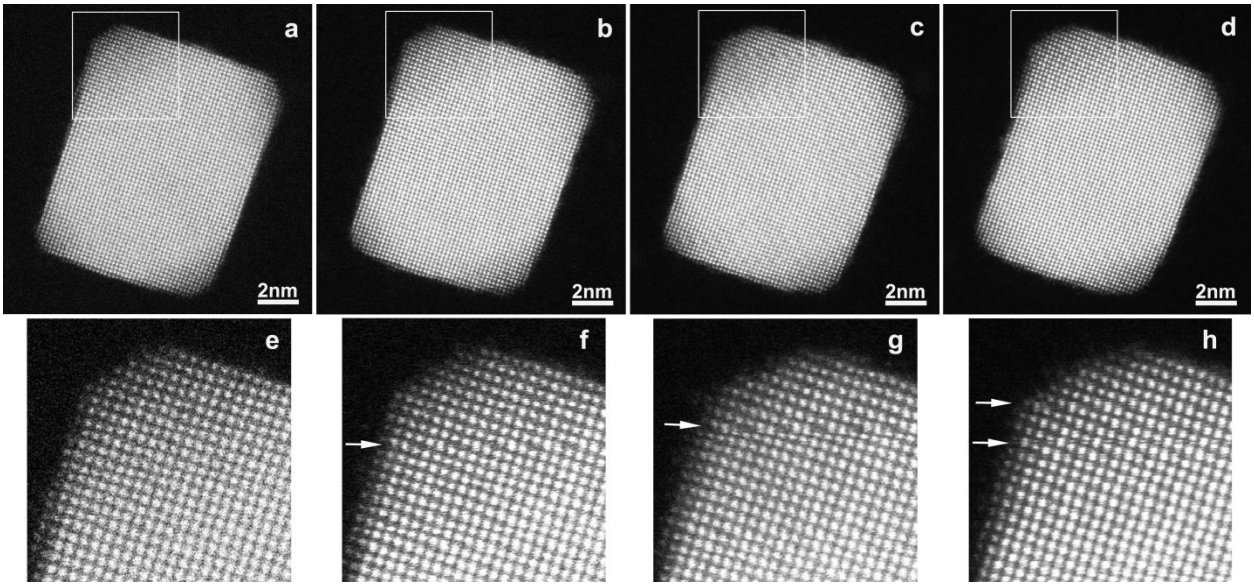

Figure S3. HAADF-STEM images of the same Pt NP at room temperature and in ultra-high vacuum on a 25 nm thick SiN support by using an acquisition time of (a) 1 s, (b) 2 s, (c) 4 s and (d) 8 s per frame. Close-up images from the upper left part of the particle at 1, 2, 4 and 8 s of acquisition are given in (e), (f), (g) and h respectively. Distortions likely related to particle rotation, indicated by white arrows, become more dominant with increasing acquisition time.

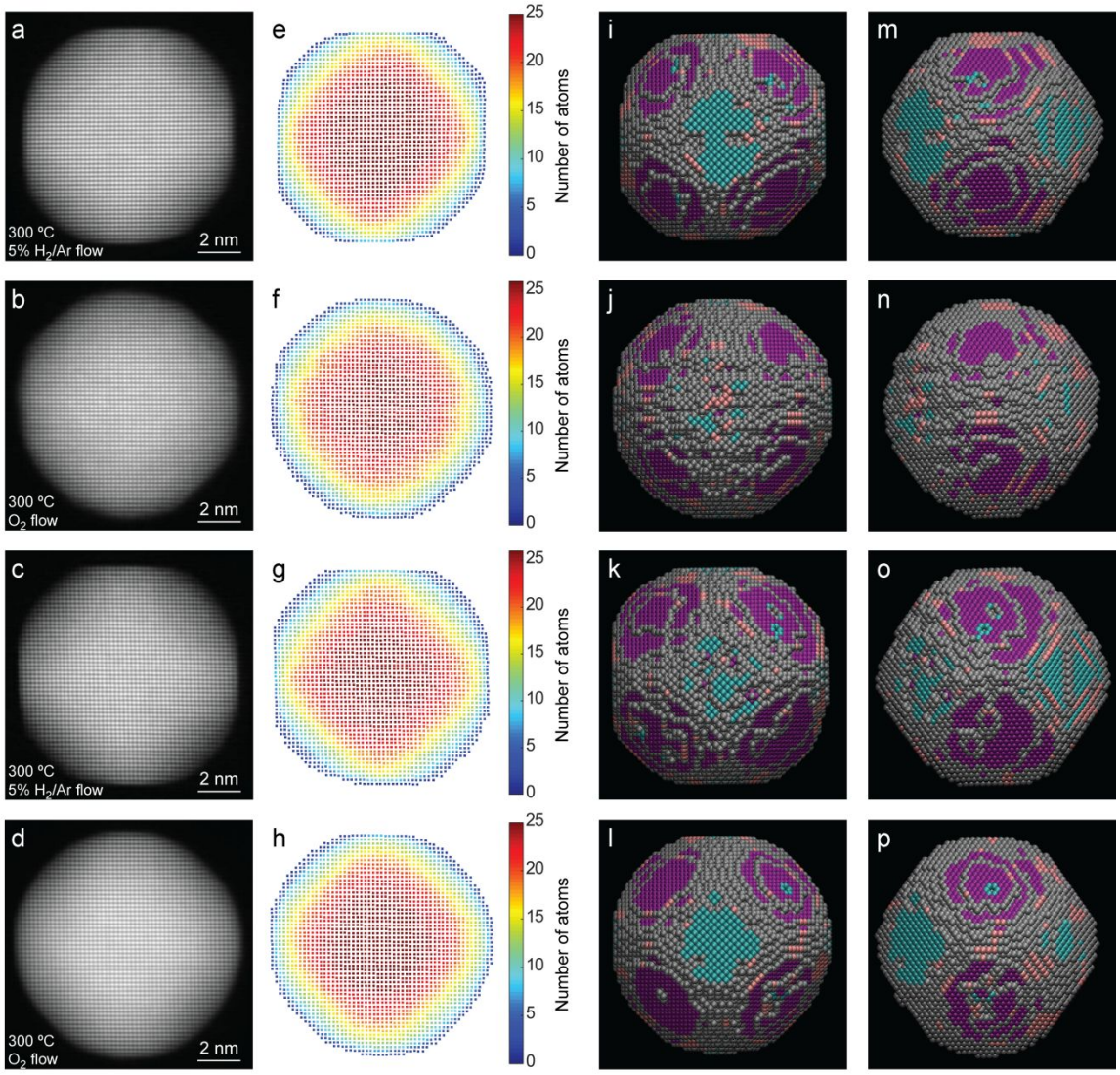

Figure S4. 2D HAADF-STEM projections (a-d), counting results (e-h) and the 3D structures along different viewing directions, of a Pt NP in different gaseous environments (i-p). The atoms are shown using different colors, according to the type of facet: blue={100}, pink={110}, purple={111}, grey=higher index.

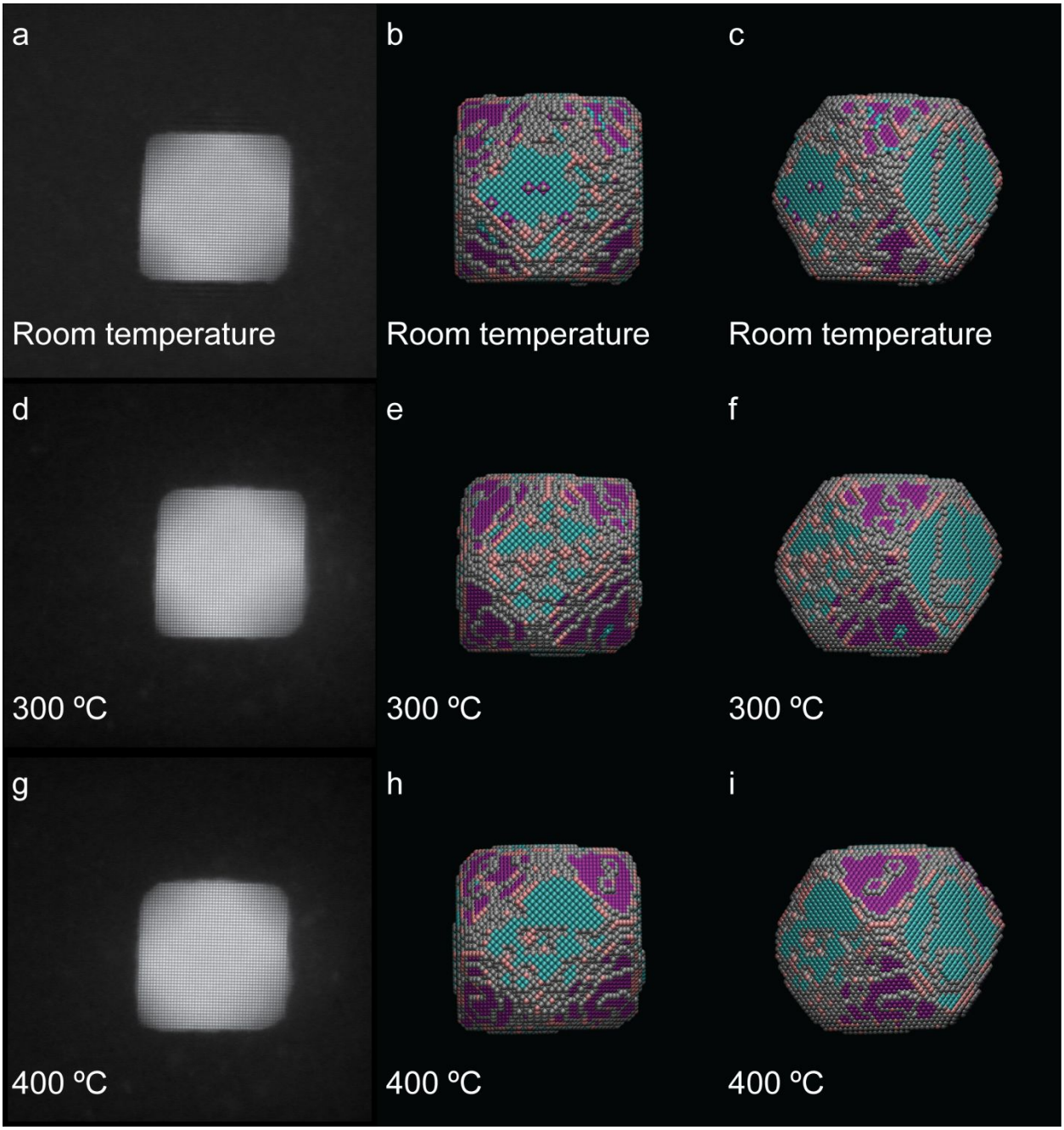

Figure S5. 2D HAADF-STEM projections and the corresponding 3D structures along different viewing directions, of a Pt NP in vacuum at room temperature (a-c), 300 ºC (d-f) and 400 ºC (g-i). The atoms are shown using different colors, according to the type of facet: blue={100}, pink={110}, purple={111}, grey=higher index. The shape of the particles is maintained while being heated in vacuum.

S4. HAADF-STEM image restoration based on a deep convolutional neural network and non-rigid registration

HAADF-STEM images may show a combination of different distortions, which depend on the instrument environment, scanning instabilities, scan-speed and electron dose.[5,6] These distortions hamper the extraction of quantitative structure information, such as the number of atoms in a given atomic column. Non-rigid registration methods using multiple successive images as an input have therefore been proposed.[7] In this study, we acquired multiple consecutive images at high speed (acquisition of 2k x 2k images with a scan time of 1s for each frame) in order to minimize beam damage, charging, and specimen rotation. As a consequence, effects of kHz-MHz frequency distortions are unfortunately very strong and often strongly correlated along the fast-scan direction. Even after applying a frame average procedure based on rigid [8] and non-rigid registration [7,9,10], these distortions persist.

To compensate for scanning distortions, we apply the concept of machine learning using a deep artificial neural network. This approach has become state-of-the-art because of its ability to learn from data by adjusting the so-called weight connections between neurons in the network during its training process. In particular, convolutional neural networks (CNNs) have resulted in a breakthrough for various tasks.[11–17] The restoration procedure we propose here is based on the use of a deep convolutional neural network that directly learns how to differentiate between distorted and undistorted HAADF-STEM images. By training the neural network, it implicitly learns to detect the presence of distortions and to correct for these, regardless the level and combination of distortions present in the image that is used as an input. The architecture that we

propose for the network consists of a stack of 12 layers, where each layer is composed of a linear convolution followed by a so-called elementwise Rectified Linear Unit.[18] All layers consist of 64 filters (except for the last one which consists of a single filter) and have a spatial filter size of 5x5. Using the Caffe framework [19], the unknown parameters are determined by minimizing the standard mean squared error employing the so-called Adam learning algorithm [20] followed by the SGD learning algorithm [21], which has been shown to have optimal convergence results.[22] Note that the input data has a size of 64x64. We train the network from scratch where the initialization of the weights has been chosen according to.[23]

Data generation

Since we are only able to collect distorted experimental images, our training dataset is based on a set of simulated undistorted and distorted images, which can be corrected on a single-shot STEM image without using any prior knowledge of the specimen. This constraint was included in order to develop a general restoration procedure. The distorted STEM image can be modelled by applying successive distortions to an undistorted image. We want to point out that the occurrence probability and the range of values of the described distortions were obtained based on the analysis of a large number of experimental STEM images.

The HAADF STEM images are generated by projecting a specimen in which each atom is modelled as a 3D Gaussian function. The specimens were generated by randomly choosing the Bravais lattice, specimen orientation, specimen thickness, lattice parameters, atomic types, amorphous composition, amorphous density, and amorphous thickness. Defects were created by removing atoms with a random probability between 0 and 20%. The brightness and contrast are randomly changed by rescaling the image and adding an offset. In order to control the level of

the counting noise during the data generation, the image is normalized in the range 0-1 by dividing by its maximum value.

In general, binning combines the information of adjacent pixel. This will lead to a change of the noise distribution and a reduction of the resolution by the binning factor. We include this effect by resizing the undistorted image intensities by a random factor of 2, 4 or 8 with a probability of occurrence of 20%. In the final step of the data generation, the distorted image is binned by the same factor. Moreover, it is known that the frame average procedure changes the noise distribution. By applying the frame average procedure to N distorted images, this effect is included in the last step of the data generation. The number N is randomly selected from a uniform integer distribution within the range $[\mathbf{2}, \mathbf{20}]$. The occurrence probability was set to 20%.

The displacement of the jitter distortions are modeled using the correlation scheme [24]

$$\Delta_{\mathbf{1}} = \frac{\boldsymbol{a_1}}{\sqrt{\mathbf{1} - \boldsymbol{\varphi}^{\mathbf{2}}}}$$

$$\Delta_{\boldsymbol{j}} = \boldsymbol{\varphi}\Delta_{\boldsymbol{j}-\mathbf{1}} + \boldsymbol{a_j}$$

where Δ is the $\boldsymbol{x}/\boldsymbol{y}$ displacement, $\boldsymbol{\varphi} \in [\mathbf{0},\mathbf{1}]$ is the correlation factor, $\boldsymbol{a_j}$ is a random number selected from a normal distribution with standard deviation $\boldsymbol{\sigma}$. In order to generate different levels of jitter distortions, $\boldsymbol{\varphi}$ and $\boldsymbol{\sigma}$ are randomly selected in the range $[\mathbf{0}, \mathbf{0.75}]$ and $[\mathbf{0}, \mathbf{0.8}]$Å, respectively. The distorted images are synthesized using the above mentioned correlation scheme combined with a bicubic interpolation. The occurrence probability of this distortion was set to 90%.

In the next step, these images are corrupted with Poisson noise which is the basic form of uncertainty associated with electron detection. This process starts by multiplying the image intensities by a random value in the range $[\mathbf{1}, \mathbf{1200}]$, followed by the generation of a random number for each pixel, which is based on the Poisson distribution. In order to go back to the original intensity scale, the generated image intensities were divided by the same scaling factor.

Fluctuations of electrons in the detector are modelled as Gaussian noise with a probability of occurrence of 50%. The standard deviation of the Gaussian noise was generated by a random number extracted in the range from 0 to the standard deviation of the undistorted image. At the saturation level, pixels lose their ability to accommodate additional charge leading to a loss of information. This effect was modelled by clipping the intensity of all pixel values having an intensity beyond a random value generated in the range from 95% to 100% of the maximum pixel intensity in the image. The occurrence probability of this effect was set to 10%.

We found out that fast scan distortion can be accurately synthetized by convolving with an exponential decaying function [5] with a random exponential factor generated in the range [0.10, 3.94]. This distortion is generated with an occurrence probability of 50%. Moreover, when X-rays hit the STEM detector, it can produce a saturation at the current pixel location. This can be modelled by including a random saturation over randomly selected pixels with an occurrence probability of 10%.

Finally, the pixel values of the distorted images are normalized in the range [0, 1] using the minimum and maximum intensity values. The undistorted images have been normalized with the same factor in order to have both undistorted and distorted images at the same scale. In order to improve the generalization of the proposed CNN architecture and to avoid overfitting, $\mathbf{10^7}$ and

$\mathbf{5 \times 10^5}$ training and validation images have been generated, respectively. After testing the reliability of this deep CNN on simulated images, the methodology was applied to our experimental dataset.

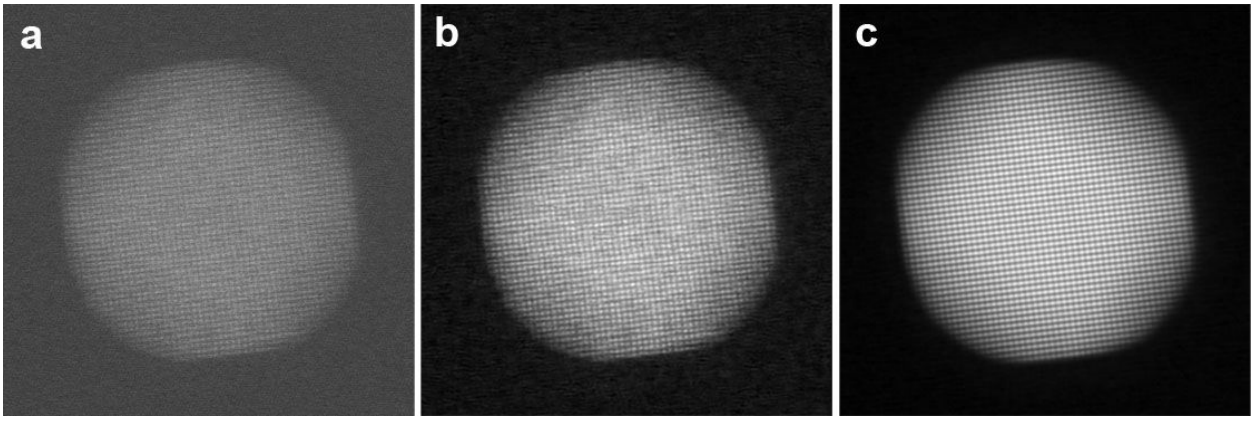

Figure S6. Pt nanoparticle under a continuous 5%H_2/Ar gas flow, at a pressure of 1 bar and a temperature of 300 ^{o}C. (a) HAADF-STEM image acquired with a frame time of 1s, distortions are clearly present. (b) HAADF-STEM image corrected using our convolutional neural network. (c) Average frame based on rigid and non-rigid registration using 5 frames.

Figure S6b shows a corrected single HAADF-STEM image, by applying our CNN to Figure S6a, presenting a high-resolution image of a Pt nanoparticle acquired at a pressure of 1 bar 5%H_2/Ar and a temperature of 300 ^{o}C and a frame time of 1 s. The optimized quality is mainly due to the compensation of the highly correlated distortions. Despite this improvement, non-linear distortions are present, which can be reduced using a non-rigid registration procedure under the assumption that the remaining distortions are uncorrelated between frames. Figure S6c shows the result of this procedure.

S5. Atom-counting

The number of atoms in the projected atomic columns was determined using a statistics-based atom-counting method.[25–27] This statistical atom-counting method is developed for application to aberration corrected HAADF-STEM images of monotype crystalline nanostructures in zone-axis. This method can be applied to nanocrystals of arbitrary shape, size, and atom type with no need for prior knowledge of the nanostructure. Trustworthy single-atom sensitivity can be achieved with this method.[26] The atom-counting here was performed using StatSTEM.[28]

The StatSTEM software enables a description of the experimental image pixel values by a sum of Gaussians which are peaked at the atomic column positions. For each Gaussian peak, the height, width, and position need to be estimated. These unknown parameters are estimated by minimizing the least squares sum. This optimization involves an iterative refinement in a huge parameters space. Important to notice is that we do take overlap between neighboring columns into account, which is particularly important for closely separated atomic columns. The width and the height of the estimated Gaussian peaks can be used to measure the volume under each Gaussian function which for HAADF-STEM imaging is very sensitive for the atom type and number of atoms in a column. These are the so-called scattering cross-sections. Since the intensity in HAADF-STEM images scales with the thickness, the scattering cross-section increases with increasing number of atoms. In contrast to the use of e.g. peak intensities, the advantage of using scattering cross-sections to count the number of atoms is its robustness to probe parameters including the defocus.[29,30] Therefore, scattering cross sections do not vary significantly with defocus.

Next, the distribution of scattering cross-sections from all the atomic columns is decomposed into overlapping normal components. The number of components and their locations can be determined using a so-called Gaussian mixture model analysis in combination with an order

selection criterion. This order selection criterion allows determining the number of statistically significant components present in the underlying cross section measures. The number of components corresponds to a minimum in the evaluation of this criterion as a function of number of components. Often this corresponds to a local minimum. A so-called Gaussian mixture model analysis allows defining the locations and the width of each Gaussian component. Next, each scattering cross-section can be assigned to the component having the highest probability for this scattering cross-section. This results in a map reflecting the number of atoms for each atomic column.

S6. Energy minimization

The counting results can be used as an input for an iterative energy minimization scheme to obtain a 3D model for the investigated structure.[31–35] Based on the atom-counting results, an initial 3D configuration is obtained by positioning the atoms in each atomic column, parallel to the beam direction, symmetrically around a central plane. The atoms are separated by a fixed distance a or a/√2 for the [100] and [110] orientation respectively (where a is the lattice parameter). In addition, prior knowledge about the FCC structure is used to assign the relative heights of neighboring columns. Molecular dynamics (MD) simulations employing the embedded atom method (EAM) [36] potential were performed using the GPU Lammps package for the relaxation of the initial 3D models.[37–39] First the initial 3D models were structurally relaxed by minimizing the energy of the system at T=0 K in order to reduce the stress in the system. Then a full MD relaxation at the experimental temperature was performed in the canonical ensemble with a time step of 2.5 fs, an equilibration period of 10 ns, and a production of 5 ns. Over the production time each atomic position has been extracted every 5 fs step. The MD simulation was carried out for a large cubic box without periodic boundary conditions so that the

surface of the nanoparticle is free. The MD relaxation procedure will relax the surface of the nanoparticle to a local minimum. The reason for this is that the experimental temperature is not large enough to overcome major constraints imposed by the atom-counting results and the symmetry in the initial configuration. The reliability of the approach was previously confirmed by comparing the outcome of this procedure to high resolution reconstructions based on multiple images acquired from different viewing directions.[32]

S7. References

(1) Lee, H.; Habas, S. E.; Kweskin, S.; Butcher, D.; Somorjai, G. A.; Yang, P. *Angew. Chemie - Int. Ed.* **2006**, *45*, 7824–7828.

(2) Creemer, J. F.; Helveg, S.; Hoveling, G. H.; Ullmann, S.; Molenbroek, A. M.; Sarro, P. M.; Zandbergen, H. W. *Ultramicroscopy* **2008**, *108*, 993–998.

(3) Jiang, Y.; Li, H.; Wu, Z.; Ye, W.; Zhang, H.; Wang, Y.; Sun, C.; Zhang, Z. *Angew. Chemie - Int. Ed.* **2016**, *55*, 12427–12430.

(4) Beyer, A.; Straubinger, R.; Belz, J.; Volz, K. *J. Microsc.* **2016**, *262*, 171–177.

(5) Buban, J. P.; Ramasse, Q.; Gipson, B.; Browning, N. D.; Stahlberg, H. *J. Electron Microsc. (Tokyo).* **2010**, *59*, 103–112.

(6) Jones, L.; Nellist, P. D. *Microsc. Microanal.* **2013**, *19*, 1050–1060.

(7) Jones, L.; Yang, H.; Pennycook, T. J.; Marshall, M. S. J.; Van Aert, S.; Browning, N. D.; Castell, M. R.; Nellist, P. D. *Adv. Struct. Chem. Imaging* **2015**, *1*, 8.

(8) Srinivasa Reddy, B.; Chatterji, B. N. *IEEE Trans. Image Process.* **1996**, *5*, 1266–1271.

(9) Wang, H.; Dong, L.; O'Daniel, J.; Mohan, R.; Garden, A. S.; Kian Ang, K.; Kuban, D. A.; Bonnen, M.; Chang, J. Y.; Cheung, R. *Phys. Med. Biol.* **2005**, *50*, 2887–2905.

(10) Cachier, P.; Pennec, X.; Ayache, N. *Tech. Rep.* **1999**, No. RR-3706, INRIA, 1–25.

(11) Krizhevsky, A.; Sutskever, I.; Geoffrey E., H. *Adv. Neural Inf. Process. Syst. 25* **2012**, *1*, 1097–1105.

(12) Shelhamer, E.; Long, J.; Darrell, T. *IEEE Trans. Pattern Anal. Mach. Intell.* **2017**, *39*, 640–651.

(13) Xie, J.; Xu, L.; Chen, E. *Nips* **2012**, *1*, 341–349.

(14) Eigen, D.; Krishnan, D.; Fergus, R. *Proc. IEEE Int. Conf. Comput. Vis.* **2013**, 633–640.

(15) Xu, L.; Ren, J. S.; Liu, C.; Jia, J. *Adv. Neural Inf. Process. Syst.* **2014**, *1*, 1790–1798.

(16) Dong, C.; Loy, C. C.; He, K.; Tang, X. *IEEE Trans. Pattern Anal. Mach. Intell.* **2014**, *38*, 295–307.

(17) Kim, J.; Lee, J. K.; Lee, K. M. *Cvpr 2016* **2016**, 1646–1654.

(18) Nair, V.; Hinton, G. E. *Proc. 27th Int. Conf. Mach. Learn.* **2010**, No. 3, 807–814.

(19) Y. Jia; Shelhamer, E.; Donahue, J.; Karayev, S.; Long, J.; Girshick, R.; Guadarrama, S.; Darrell, T. *Proc. 22nd ACM Int. Conf. Multimed.* **2014**, 675–678.

(20) Kingma, D. P.; Ba, J. L. *Int. Conf. Learn. Represent. 2015* **2015**, 1–15.

(21) Bottou, L. *Neural Networks: Tricks of the Trade* **2012**, *1*, 1–14.

(22) Wu, Y.; Schuster, M.; Chen, Z.; Le, Q. V.; Norouzi, M.; Macherey, W.; Krikun, M.; Cao, Y.; Gao, Q.; Macherey, K.; et al. http://arxiv.org/abs/1609.08144. **2016**.

(23) He, K.; Zhang, X.; Ren, S.; Sun, J. *Proc. IEEE Int. Conf. Comput. Vis.* **2015**, 1026–1034.

(24) Walker, G. *Proc. R. Soc. A Math. Phys. Eng. Sci.* **1931**, *131*, 518–532.

(25) Van Aert, S.; Batenburg, K. J.; Rossell, M. D.; Erni, R.; Van Tendeloo, G. *Nature* **2011**, *470*, 374–377.

(26) Van Aert, S.; De Backer, A.; Martinez, G. T.; Goris, B.; Bals, S.; Van Tendeloo, G.; Rosenauer, A. *Phys. Rev. B - Condens. Matter Mater. Phys.* **2013**, *87*, 64107.

(27) De Backer, A.; Martinez, G. T.; Rosenauer, A.; Van Aert, S. *Ultramicroscopy* **2013**, *134*, 23–33.

(28) De Backer, A.; van den Bos, K. H. W.; Van den Broek, W.; Sijbers, J.; Van Aert, S. *Ultramicroscopy* **2016**, *171*, 104–116.

(29) E, H.; MacArthur, K. E.; Pennycook, T. J.; Okunishi, E.; D'Alfonso, A. J.; Lugg, N. R.; Allen, L. J.; Nellist, P. D. *Ultramicroscopy* **2013**, *133*, 109–119.

(30) Martinez, G. T.; De Backer, A.; Rosenauer, A.; Verbeeck, J.; Van Aert, S. *Micron* **2014**, *63*, 57–63.

(31) Geuchies, J. J.; Van Overbeek, C.; Evers, W. H.; Goris, B.; De Backer, A.; Gantapara, A. P.; Rabouw, F. T.; Hilhorst, J.; Peters, J. L.; Konovalov, O.; et al. *Nat. Mater.* **2016**, *15*, 1248–1254.

(32) De Backer, A.; Jones, L.; Lobato, I.; Altantzis, T.; Goris, B.; Nellist, P. D.; Bals, S.; Van Aert, S. *Nanoscale* **2017**, *9*, 8791–8798.

(33) Peters, J. L.; Van Den Bos, K. H. W.; Van Aert, S.; Goris, B.; Bals, S.; Vanmaekelbergh, D. *Chem. Mater.* **2017**, *29*, 4122–4128.

(34) Jones, L.; Macarthur, K. E.; Fauske, V. T.; Van Helvoort, A. T. J.; Nellist, P. D. *Nano Lett.* **2014**, *14*, 6336–6341.

(35) Bals, S.; Van Aert, S.; Romero, C. P.; Lauwaet, K.; Van Bael, M. J.; Schoeters, B.; Partoens, B.; Yücelen, E.; Lievens, P.; Van Tendeloo, G. *Nat. Commun.* **2012**, *3*.

(36) Foiles, S. M.; Baskes, M. I.; Daw, M. S. *Phys. Rev. B* **1986**, *33*, 7983–7991.

(37) Brown, W. M.; Wang, P.; Plimpton, S. J.; Tharrington, A. N. *Comput. Phys. Commun.* **2011**, *182*, 898–911.

(38) Brown, W. M.; Kohlmeyer, A.; Plimpton, S. J.; Tharrington, A. N. *Comput. Phys. Commun.* **2012**, *183*, 449–459.

(39) Michael Brown, W. M.; Yamada, M. *Comput. Phys. Commun.* **2013**, *184*, 2785–2793.